



An Anomalous Cosmic-Ray Mediated Termination Shock: Implications for Energetic Neutral Atoms

M. Kornbleuth¹ , M. Opher¹ , G. P. Zank^{2,3} , B. B. Wang² , J. Giacalone⁴ , M. Gkioulidou⁵ , and K. Dialynas⁶

¹Astronomy Department, Boston University, Boston, MA 02215, USA; kmarc@bu.edu

²Center for Space Plasma and Aeronomic Research (CSPAR), University of Alabama in Huntsville, Huntsville, AL 35899, USA

³Department of Space Science, University of Alabama in Huntsville, Huntsville, AL 35899, USA

⁴Lunar & Planetary Laboratory, University of Arizona, Tucson, AZ 85721, USA

⁵Applied Physics Laboratory, Johns Hopkins University, Laurel, MD 20723, USA

⁶Office of Space Research and Technology, Academy of Athens, 10679 Athens, Greece

Received 2022 October 30; revised 2023 February 6; accepted 2023 February 6; published 2023 February 22

Abstract

The Voyager 2 crossing of the termination shock indicated that most of the upstream energy from the thermal solar wind ions was transferred to pickup ions (PUIs) and other energetic particles downstream of the shock. We use hybrid simulations at the termination shock for the Voyager 2, flank, and tail directions to evaluate the distributions of different ion species downstream of the shock over the energy range of 0.52–55 keV. Here, we extend the work of Gkioulidou et al., which showed an energy-dependent discrepancy between modeled and energetic neutral atom (ENA) observations, and fit distributions to a hybrid model to show that a population of PUIs accelerated via diffusive shock acceleration (DSA) to become low-energy anomalous cosmic rays (ACRs) can bridge the gap between modeled and observed ENA fluxes. Our results with the inclusion of DSA via hybrid fitting give entirely new and novel evidence that DSA at the termination shock is likely to be an important physical process. These ACRs carry a significant fraction of the energy density at the termination shock (22%, 13%, and 19% in the Voyager 2, flank, and tail directions, respectively). Using these ACRs in global ENA modeling of the heliosphere from 0.52 to 55 keV, we find that scaling factors as large as 1.8–2.5 are no longer required to match ENA observations at energies of ~1–4 keV. Large discrepancies between modeled and observed ENAs only remain over energies of 4–20 keV, indicating that there may be a further acceleration mechanism in the heliosheath at these energies.

Unified Astronomy Thesaurus concepts: [Heliosphere \(711\)](#); [Solar system \(1528\)](#); [Heliopause \(707\)](#); [Heliosheath \(710\)](#); [Termination shock \(1690\)](#); [Pickup ions \(1239\)](#); [Solar wind \(1534\)](#); [Interstellar medium \(847\)](#); [Magnetohydrodynamical simulations \(1966\)](#); [Magnetohydrodynamics \(1964\)](#)

1. Introduction

Pickup ions (PUIs) are the dominant thermodynamic population in the heliosheath. Richardson et al. (2008) observed that at the Voyager 2 crossing of the termination shock, the thermal solar wind ions were heated modestly and remained supersonic downstream of the shock. Specifically, the plasma measurements at Voyager 2 and extrapolations of Voyager 1 energetic particle measurements to pickup ion energies inside the HS showed that only ~20% of the upstream energy density went into heating the downstream thermal plasma, whereas the remaining ~80% went into heating the PUIs and >15% was transferred to the >28 keV protons. This behavior is consistent with the predictions from Zank et al. (1996), who showed that the PUIs would be predominantly heated and that the thermal solar wind ions would remain comparatively cold. Zank et al. (1996), and subsequently Zank et al. (2010), concluded that ~65% of the upstream dynamic pressure at the shock goes into heating PUIs and ~15% of the thermal solar wind energy density is transferred to protons with energies >28 keV. Observations indicate that the nonthermal PUI plasma is thermodynamically dominant in the inner heliosheath (Krimigis et al. 2010; Roelof et al. 2010;

Livadiotis et al. 2013; Decker et al. 2015; Dialynas et al. 2019, 2020; Livadiotis et al. 2022), which is supported theoretically (Zank et al. 1996, 2010) and via magnetohydrodynamic (MHD) modeling (Malama et al. 2006; Zank et al. 2010, 2014a; Pogorelov et al. 2016; Opher et al. 2020).

PUIs in the heliosheath are observed indirectly through their production of energetic neutral atoms (ENAs). The IBEX-Hi instrument (Funsten et al. 2009) onboard the Interstellar Boundary Explorer (McComas et al. 2009) observes hydrogen ENAs originating in the heliosphere and beyond from energies of 0.52–6 keV (McComas et al. 2020; Galli et al. 2022). Additionally, the Ion and Neutral Camera (INCA; Krimigis et al. 2009) onboard the late Cassini spacecraft observed ENAs in the heliosphere from 5.2 to 55 keV (Dialynas et al. 2022). At these energies, PUIs energized at the termination shock and beyond are the primary source for ENA production.

Currently, global ENA models are unable to replicate ENA flux observations quantitatively (Kleimann et al. 2022) at energies ~1–6 keV. ENA modeling requires that plasma quantities in the MHD models (in which the plasma distribution is treated as a single distribution function—either as a Maxwellian or as a kappa distribution, e.g., Heerikhuisen et al. 2008) be postprocessed as a full non-Maxwellian distribution. This is usually done by partitioning the MHD plasma quantities to represent multiple ion species in postprocessing downstream of the termination shock to properly model ENAs. ENA models that use a combined



Original content from this work may be used under the terms of the [Creative Commons Attribution 4.0 licence](#). Any further distribution of this work must maintain attribution to the author(s) and the title of the work, journal citation and DOI.

Maxwellian approach to replicate a kappa distribution in the solar wind plasma (Zank et al. 2010) for three ion populations at the termination shock (thermal ions, “transmitted PUIs” which have sufficient energy to overcome the cross-shock potential of the termination shock, and “reflected PUIs” which do not initially have sufficient energy to overcome the cross-shock potential of the termination shock and are reflected at the shock) require a scaling factor to compare directly with IBEX-Hi observations ranging from 1.8 to 2.5 (Zirnstein et al. 2017; Kornbleuth et al. 2018, 2020; Shrestha et al. 2021) regardless of solar wind conditions (steady state or with the inclusion of realistic solar cycle). Baliukin et al. (2020) use a kinetic model for PUIs which models the propagation of PUIs in the heliosheath and includes the change in PUI energy due to $\nabla \cdot \mathbf{v}$, where \mathbf{v} is the bulk velocity of the plasma, in the heliosheath. Even with the inclusion of $\nabla \cdot \mathbf{v}$ that captures the change in PUI density in the heliosheath due to adiabatic heating, Baliukin et al. (2020) find an overprediction of ENA flux for a steady state heliosphere and is obliged to use a scaling factor of 0.67 to directly compare with IBEX-Hi observations. Using a time-dependent MHD solution of the heliosphere with realistic solar cycle conditions, Baliukin et al. (2020) observed good agreement between modeled flux and IBEX-Hi observations at the 1.11 and 1.74 keV energy bands, but they underpredict observations at the 2.73 and 4.29 keV energy bands. However, in their work they only include a transmitted PUI population which does not strongly contribute to ENA production beyond 2 keV.

Idealized, single-fluid MHD models cannot accurately capture directly the partitioning of energy downstream of the termination shock. The use of a hybrid model as a reference is important because hybrid models can describe how energy from upstream of the termination shock can be distributed downstream. Giacalone et al. (2021) perform a hybrid simulation of the termination shock for the Voyager 2, flank, and tail directions based on the model of Giacalone & Decker (2010). Hybrid simulations capture the ion dynamics as well as turbulence at larger scales to better describe the physics of the termination shock up to ion energies of 50 keV. Giacalone & Decker (2010) show that such simulations produce a good agreement with the lower energy channels of Voyager 2 LECP measurements. Gkioulidou et al. (2022) used an ENA model with a combination of different ion populations to reproduce the hybrid ion fluxes of Giacalone et al. (2021) for the Voyager 2 direction. The ion distribution downstream of the termination shock was treated as two separate populations: transmitted PUIs with a kappa distribution and a combined reflected and accelerated PUI population with a kappa distribution. The authors found that the modeled ENAs, for their best-fit model, differed from the observed ENAs of IBEX-Hi and INCA by an energy-dependent scaling factor. The discrepancy between modeled and observed ENA flux seen in other ENA models remained in the work of Gkioulidou et al. (2022), despite improved modeling of the ion distribution downstream of the termination shock according to the hybrid model of Giacalone et al. (2021). The authors concluded that some additional heating, or acceleration, of the PUI distribution in the heliosheath was necessary to replicate the data trend for all energies, especially at energies from 4 to 10 keV.

Zirnstein et al. (2022) were able to quantitatively replicate the IBEX-Hi flux in the Voyager 2 direction via ENA modeling by including flux contributions from PUI heating at the

termination shock, heating in the heliosheath (characterized as the region between the termination shock and heliopause), and from the outer heliosheath (characterized by the secondary ion population beyond the heliopause). They model the distribution of PUIs by assuming a generalized filled-shell distribution (McComas et al. 2021) and found that PUI heating at the termination shock is important for matching observations from IBEX-Hi. However, one limitation of this model was that the heating of PUIs across the termination shock was modeled via a polytropic heating relation. The authors did find that particle-in-cell and test particle simulations have indicated a polytropic heating index ranging from ~ 2.0 to 2.5, which is close to the results of Zirnstein et al. (2022).

In this work, we expand on the work of Gkioulidou et al. (2022), separating the reflected and accelerated PUIs, which Giacalone et al. (2021) characterize as low-energy ACRs for energies >5 keV, to investigate the implications of PUI acceleration at the termination shock on ENAs. We model the best-fit ion distributions to the hybrid simulation of Giacalone et al. (2021). We model ion and ENA fluxes for all three directions (Voyager 2, flank, and tail) instead of just the Voyager 2 direction. In Section 2, we discuss a modeling procedure based on a theoretical model by Wang et al. (2023) to replicate the ion fluxes from Giacalone et al. (2021) and present comparisons between our modeled distributions and the hybrid results. In Section 3, we apply our ion flux distributions in our ENA model to compare with IBEX-Hi and INCA observations as in Gkioulidou et al. (2022). In Section 4, we present a summary of our findings.

2. Simulating the Ion Flux at the Termination Shock

In modeling the ion flux at the termination shock, we follow the work of Gkioulidou et al. (2022) and find the best-fit scenario to match the hybrid simulation results of the energized thermal solar wind and PUI distribution functions downstream of the termination shock from Giacalone et al. (2021). In Giacalone et al. (2021), the hybrid simulation assumed physical quantities such as the average proton velocity, magnetic field, electric field, and others that depended on two spatial coordinates, although all the components of the vectors were included. The simulation incorporates a self-consistent, kinetic treatment of thermal solar wind protons and PUIs, with a fluid treatment of massless, charge-neutralizing solar wind electrons. Additionally, there is an average component and a turbulent component for the initial magnetic field and bulk plasma velocity. The hybrid simulation is applied to three locations at the termination shock: the Voyager 2 direction, the flank, and the tail. The hybrid model is limited by the simulation domain size and time, and therefore decreases in accuracy around energies of 50 keV and above. Another limitation of the hybrid model is that a spherical shell distribution is assumed for the PUIs upstream of the termination shock, which does not account for the adiabatic cooling effect with distance from the Sun (Vasyliunas & Siscoe 1967) or the nonadiabatic effects observed by the SWAP instrument aboard New Horizons (McComas et al. 2021). However, Giacalone et al. (2021) note they do not expect the general conclusions of their work would change by using a more realistic distribution of the PUIs since PUIs are suprathermal and will manage to dominate the pressure even with a broader distribution. The cross-shock potential determines the PUI velocity normal to the shock front that will be reflected. As illustrated in Zank et al. (1996), the

volume of an upstream PUI-filled shell that will be reflected is not much larger (unless the cross-shock potential is perhaps unrealistically large) than might be expected from a shell distribution. Where the change will be largest is that more PUIs will be transmitted for the filled shell than the simple shell distribution. Thus, the downstream lower energy PUI distribution will be larger than in the hybrid model. The primary difference will be a larger number of less energetic PUIs downstream than predicted by a thin shell. This population is also unlikely to be DSA accelerated since they do not reach the injection energy. This would therefore produce more lower energy ENAs and fewer higher energy (>5 keV) ENAs, resulting in a softer ENA spectrum in the ~ 1 – 5 keV range and a harder spectrum in energies >5 keV.

In this work, we focus on the PUI flux from Giacalone et al. (2021) for the three directions and attempt to distinguish the different contributing PUI populations that produce the results of the hybrid simulation. To do so, we test two types of total particle distributions to find the distributions that best represent the physics of the hybrid simulation in the shock rest frame. For both methods, we assume a Maxwellian distribution for the transmitted and reflected PUIs, as for the one case considered by Zank et al. (2010). Here we note that the termination shock in the hybrid model of Giacalone et al. (2021) has a thickness on the order of the ion inertial length and not on the order of the electron inertial length as considered by Zank et al. (1996, 2010). Therefore, the reflected PUI population noted here is regarded as a population that is accelerated to ~ 3 – 5 keV within the termination shock, but not necessarily due to the cross-shock potential. For the first method (two-kappa method), we fit two additional energized ion populations via kappa distributions given by Prested et al. (2008)

$$f(v) = \frac{n\Gamma(\kappa + 1)}{w_0^3 \pi^{3/2} \kappa^{3/2} \Gamma(\kappa - 1/2)} \left[1 + \frac{v^2}{\kappa w_0^2} \right], \quad (1)$$

where $w_0 = \sqrt{2T(\kappa - 3/2)/(m_p \kappa)}$. This function was first proposed by Vasyliunas (1968) and is described in this work using the notation of Collier (1995). For a sufficiently steep power-law tail ($\kappa \rightarrow \infty$), the distribution approaches a Maxwellian. Here, v is the ion velocity in the rest frame of the shock as in Giacalone et al. (2021), n is the number density of the ions, and T is the ion temperature. For this method, we vary the density and energy fractions for the transmitted and reflected PUIs, as well as the two additional populations described via kappa distributions. We also vary κ for each kappa distribution to best fit the hybrid results. We note that this method does not add particles to the model as the kappa distributions are included as fits to the hybrid results.

The second method (referred to as the ZW method), following the work of Wang et al. (2023), extends the method of Zank et al. (2010) that assumes three ion populations modeled as Maxwellian distributions: thermal solar wind ions, transmitted PUIs, and reflected PUIs. Wang et al. (2023) modify the reflected PUI population to incorporate the further acceleration of a fraction of the reflected PUIs at the termination shock via diffusive shock acceleration (DSA) due to turbulence, thereby becoming ACRs. The reflected PUIs are

modeled via a Maxwellian distribution as

$$f(v) = \frac{(1 - \xi)nm_p^{3/2}}{(2\pi k_B T)^{3/2}} e^{-\frac{mv_p^2}{2k_B T}}, \quad (2)$$

where ξ is the fraction of reflected PUIs accelerated at the termination shock, m_p is the proton mass, and k_B is the Boltzmann constant. The accelerated PUIs are modeled via (Wang et al. 2023)

$$f(v) = \frac{\xi n(\delta - 3)(q - 3)}{4\pi v_l^3(q - \delta)} \times \begin{cases} (v/v_l)^{-\delta} - (v/v_l)^{-q}, & \text{if } v_l < v \leq v_m \\ [(v_m/v_l)^{q-\delta} - 1] - (v/v_l)^{-q}, & \text{if } v > v_m \end{cases} \quad (3)$$

where δ is the power-law index related to multiply reflected ion (MRI) acceleration (Zank et al. 1996), and q relates the PUI acceleration to the shock compression ratio (R) via $q = 3R/(R - 1)$. Additionally, v_l is the minimal particle velocity for DSA, and v_m is the maximal particle velocity of multiply reflected particles that undergo further acceleration by DSA. Giacalone & Decker (2010) suggested that shock drift plays a significant role in the acceleration of PUIs to higher energies. The primary method by which the particles gain energy at the shock is by drifting along the shock front, due to the ∇B drift, in the same direction as the motional electric field. This is known as shock drift acceleration and, in the presence of turbulent magnetic fields and associated pitch-angle scattering, is a subset of the more-general term ‘‘diffusive shock acceleration.’’

For these different distributions, we vary the density and energy fractions of the different populations with increments of $\Delta(n_i/n_p) = 0.01$ and $\Delta(E_i/E_p) = 0.01$ to find the best-fit parameters, where n and E are the ion density and energy, respectively, i denotes the ion species, and p denotes the plasma. We also vary other free parameters depending on the form of the distribution, with increments based on the potential range of the parameter. To determine the best-fit parameters, we evaluate the combination of each set of parameters for a given direction relative to the hybrid results for the same direction via

$$\chi = \sum_{w=0}^N \frac{[\log_{10}(J_{\text{model}}(E_w)) - \log_{10}(J_{\text{hybrid}}(E_w))]^2}{N}, \quad (4)$$

where J is the total ion flux at a particular energy (E) and N is the number of sampled energies. The best-fit parameters are determined by the parameters that minimize Equation (4).

In the top left panel of Figure 1, we show a comparison of our different methods relative to the hybrid model and observationally derived ion fluxes for IBEX-Hi and INCA from Dialynas et al. (2020). We find that the two-kappa method is able to best replicate the results of the hybrid model (IBEX-Hi energies: $\langle \text{model/hybrid} \rangle = 1.0011 \pm 0.0237$; INCA energies: $\langle \text{model/hybrid} \rangle = 1.0093 \pm 0.1078$ in Voyager 2 direction). For the best-fit ZW method with a power-law index of $\delta = 9.5$ (herein, referred to as the ZW9 method), there is also agreement on average with the hybrid results (IBEX-Hi energies: $\langle \text{model/hybrid} \rangle = 1.0010 \pm 0.0233$; INCA energies: $\langle \text{model/hybrid} \rangle = 1.0312 \pm 0.3334$ in Voyager 2 direction),

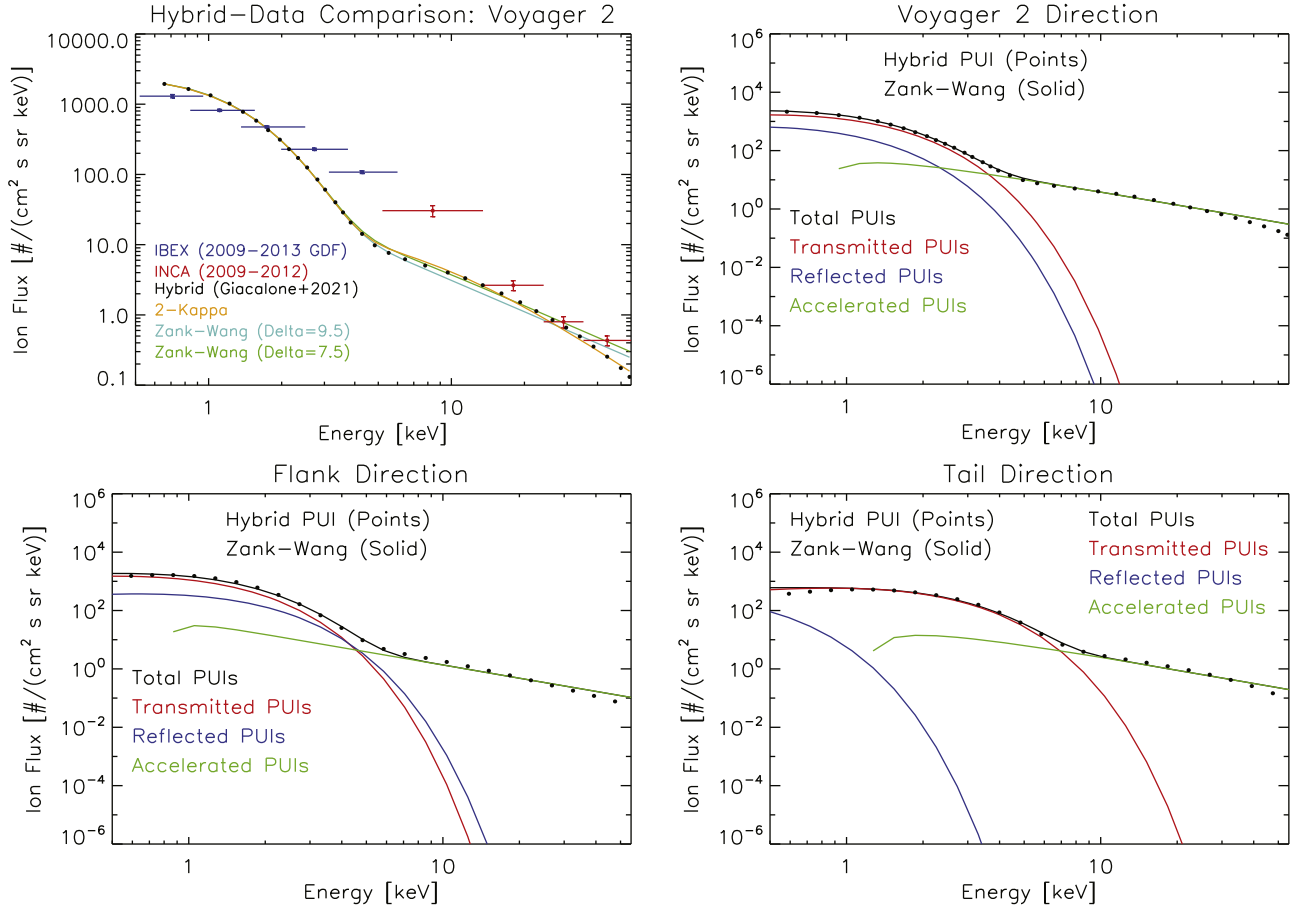


Figure 1. Ion fluxes inferred from observations and derived from models. Top left: ion flux inferred from IBEX-Hi (blue dots) and INCA (red dots) observations averaged over the years 2009–2012 assuming $n_H = 0.12 \text{ cm}^{-3}$ in the heliosheath and a heliosheath thickness of 35 au in the Voyager 2 direction (Dialynas et al. 2020). The lines correspond to best-fit model results to the hybrid model of Giacalone et al. (2021); black dots) for a two-kappa approximation of the flux (orange) and using the ZW method with $\delta = 9.5$ (ZW9 method—turquoise) and $\delta = 7.5$ (ZW7 method—green). Also included are relative ion contributions for the ZW7 method relative to the hybrid model for the Voyager 2 direction (top right), flank direction (bottom left), and tail direction (bottom right). In these plots, the black dots correspond to the hybrid model, and the red, blue, green, and black lines correspond to the ion fluxes from the transmitted, reflected, accelerated/reflected, and combined PUIs, respectively.

yet this method produces more variation with respect to the hybrid model at the highest INCA energies. One limitation of the hybrid model is that in order to accurately model the high-energy component of the plasma, the simulation domain must be large enough to be able to resolve the scattering mean-free path and scattering time for a particular ion population. For the model by Giacalone et al. (2021), the domain used is determined to be sufficiently adequate to model the formation of the high-energy tail of the ion distribution up to approximately 50 keV. Because this limit coincides with the highest energy channel of INCA, we note a potential source of error in the highest energies of the hybrid model used in this work. Therefore, we introduce an additional method, the ZW method with a power-law index of $\delta = 7.5$ (herein, referred to as the ZW7 method). While this method does not present a good agreement to the hybrid results at energies > 30 keV, the ZW7 method actually presents better agreement with the INCA data at energies < 30 keV, and identical agreement at the IBEX-Hi energies. Additionally, the ZW7 method produces an ion flux that is able to replicate the ion flux from the highest INCA energy channel. Therefore, for the remainder of this work we will use the ZW7 method.

In Table 1, we present the best-fit parameters relative to the hybrid results used in the ZW7 method for the Voyager 2,

Table 1
Best-fit Parameters Relating the ZW7 Model to Hybrid Results

Parameter	Voyager 2	Flank	Tail
n_{tr}/n_p	0.18	0.24	0.20
n_{ref}/n_p	0.07	0.07	0.05
ξ	0.08	0.06	0.12
E_{tr}/E_p	0.56	0.61	0.72
E_{ref}/E_p	0.18	0.22	0.03
E_{accel}/E_p	0.22	0.13	0.19
δ	7.5	15.5	7.5
E_l [keV]	0.80	0.80	1.20
E_m [keV]	25.00	7.00	12.00

Note. Included are the density ratios (n_i/n_p) and energy ratios (E_i/E_p) for the different PUI populations relative to the plasma (subscript p). The subscripts tr, ref, and accel refer to the transmitted, reflected, and accelerated/reflected PUIs, respectively. ξ is the fraction of reflected PUIs accelerated at the termination shock, δ is the power-law index for the ZW7 method, and E_l and E_m are the minimum and maximum energies for reflected PUI acceleration, respectively.

flank, and tail directions. For the free parameters, we have the transmitted PUI density fraction (n_{tr}), the reflected PUI density fraction (n_{ref}), the transmitted PUI energy fraction (E_{tr}), and the reflected PUI energy fraction (E_{ref}) relative to the plasma.

Additionally, we have the fraction of reflected PUIs that are accelerated via diffusive shock acceleration at the termination shock (ξ), the minimum (E_i) and maximum (E_m) energies of particles that will undergo further acceleration by DSA at the termination shock, and the power-law index for the accelerated PUIs (δ). The energy fraction of the accelerated PUIs (E_{acc}) is deduced from energy conservation. These parameters are used in the modeled ion fluxes shown in the top right and bottom panels of Figure 1, where the ion flux from each population is shown, as well as the total combined ion flux relative to the hybrid model.

In this updated work to Gkioulidou et al. (2022), we improve our fit to the hybrid model of Giacalone et al. (2021) by better capturing the different acceleration mechanisms that are at play at the termination shock by separating the “energized” PUI population from Gkioulidou et al. (2022) into two distinct populations: PUIs that get accelerated by cross-shock potential 3–5 keV and PUIs accelerated by diffusive shock acceleration due to turbulence at the shock to energies above 5 keV. Here, we capture the ion spectrum between 1 and 3 keV with transmitted PUIs and between 3 and 5 keV with the “reflected” PUIs. The “reflected” PUIs refer to PUIs that undergo acceleration within the termination shock (3–5 keV), but are not necessarily due to the cross-shock potential. We now also fit a population of low-energy ACRs to the hybrid model, which is accelerated via DSA from turbulence and is created from the reflected PUIs, using the model of Wang et al. (2023). Through this method of better matching the higher energy ion spectrum with the low-energy ACRs, we remove lower energy ions from the reflected PUI distribution at 3–5 keV, which also affects our fitting.

By better capturing the acceleration at the termination shock through the division of the “energized” PUIs used in Gkioulidou et al. (2022) into “reflected” PUIs and low-energy ACRs, we find an improvement for the fitting of the hybrid results. In comparison with the parameters used in Gkioulidou et al. (2022), we then find that the parameters in Table 1 have notably changed for all of the different PUI populations: the plasma density partition leads to a decrease in the transmitted PUI fraction from 23% to 18% in the Voyager 2 direction, while the reflected PUI population, and therefore the low-energy ACRs which are accelerated from the reflected population, increase in their total density fraction from 3% to 7%. Whereas in Gkioulidou et al. (2022) the transmitted PUIs were the dominant population from ~ 1 to 4 keV, here we find that while the combined density fraction of the transmitted and reflected PUIs is similar to the transmitted PUI density fraction from Gkioulidou et al. (2022), we now have substantially more energy from the combined populations (74%) than the transmitted PUIs carried in Gkioulidou et al. (2022) alone (50%), which yields a better fit.

Notably, while we find a relatively small fraction of the reflected PUIs undergo additional acceleration at the termination shock ranging from 6% to 12%, the energy fraction of the accelerated component ranges from 13% to 22%. For the Voyager 2 and tail directions in particular, we find that the energy budget for the accelerated PUIs is comparable to or higher than the reflected PUIs. While previous works (Zank et al. 2010; Zirnstein et al. 2017; Kornbleuth et al. 2018, 2020) have assumed a reflected PUI population that is hotter than the transmitted PUIs, here we find in the Voyager 2 and tail directions that the transmitted PUIs ($T_r/T_p = 3.11, 3.6,$

respectively) are hotter than the reflected PUIs ($T_{\text{ref}}/T_p = 2.80, 0.68,$ respectively). This can be attributed to the removal of high-energy PUIs from the original reflected PUI distribution as a new accelerated component is created. As noted in Giacalone et al. (2021), ACRs are considered to cover energies > 5 keV in the suprathermal tail of the total ion flux. Therefore, based on these results we find that the ACRs are an important population at the termination shock and are likely to mediate the shock structure as suggested by Florinski et al. (2010).

3. Simulating the ENA Flux in the Heliosheath

For this section, we use an updated form of the ENA model from Kornbleuth et al. (2018, 2020), which was used in Gkioulidou et al. (2022). Here, instead of calculating the PUI fractions at the termination shock based on the method described in (Lee et al. 2009; Zirnstein et al. 2017), we extrapolate the best-fit parameters from the ZW7 method for the Voyager 2, flank, and tail directions to all directions and model the downstream PUI distributions in the downstream plasma frame. Because our fits are done in the shock frame, for the downstream plasma frame we shift our distribution functions by the relative velocity between the shock and downstream plasma (approximately 143 km s^{-1} in the Voyager 2 direction) to transform our frame of reference. For example, in the Voyager 2 direction we shift our particles in our distribution by 143 km s^{-1} . In comparison, the thermal speed of the PUIs is approximately 380 km s^{-1} in the Voyager 2 direction. While the thermal speed is notably larger than the translational speed used to shift the frame of reference, our distribution functions are isotropic in the shock frame and anisotropic in the downstream plasma frame, in contrast with the typical assumption of models of the heliosheath, which utilize an isotropic distribution in the downstream plasma frame. We need to extract these parameters along the termination shock in order to model how the density and energy of PUIs varies along the termination shock because of the nonradial plasma flow in the heliosheath, which results in other shock positions contributing to the ENA flux for a given direction via flow deflection. While we do not have a reference point higher in latitude than Voyager 2 (e.g., we do not have a specific fit to the heliosphere poles), as noted in Giacalone et al. (2021) we do not expect a difference in the intensity of the accelerated PUI tail by the termination shock in the polar regions compared to the flank given the similar termination shock distances. Additionally, the accelerated PUI intensity may be related to the injection at the shock and turbulence; however, the quasi-parallel part of the termination shock in the poles is likely very small as noted by Jokipii & Kota (1989) due to the transverse components of the turbulent magnetic field dominating the radial field at large distances from the Sun (Jokipii & Parker 1968). As in Nakanotani et al. (2020) and Giacalone et al. (2021), in our extrapolation the fit that we use is based on the radial distance to the termination shock. We use exponential fits to best capture how the parameters vary at locations along the termination shock that were not modeled explicitly by Giacalone et al. (2021). We find the parameters vary as:

$$r' = \ln \left(\frac{r_{\text{TS}}(\theta, \phi)}{r_{\text{TS}}(\theta_{V2}, \phi_{V2})} \right) \quad (5)$$

$$n_{\text{tr}}(r') = \exp(-4.6596r_{\text{TS}}^2 + 2.46160r_{\text{TS}} - 1.71480) \quad (6)$$

$$n_{\text{ref}}(r') = \exp(-2.27104r_{\text{TS}}^2 + 0.395963r_{\text{TS}} - 2.65926) \quad (7)$$

$$E_{\text{tr}}(r') = \exp(0.101026r_{\text{TS}}^2 + 0.472896r_{\text{TS}} - 0.579818) \quad (8)$$

$$E_{\text{ref}}(r') = \exp(-15.8367r_{\text{TS}}^2 + 3.91212r_{\text{TS}} - 1.71480) \quad (9)$$

$$\xi(r') = \exp(8.10281r_{\text{TS}}^2 + 3.06275r_{\text{TS}} - 2.52573) \quad (10)$$

$$E_l(r') = \exp(2.73671r_{\text{TS}}^2 - 0.477155r_{\text{TS}} - 0.223144) \quad (11)$$

$$E_m(r') = \exp(18.7905r_{\text{TS}}^2 - 10.5773r_{\text{TS}} - 3.21888) \quad (12)$$

$$\delta(r') = \exp(-13.5408r_{\text{TS}}^2 + 6.52448r_{\text{TS}} - 2.01490) \quad (13)$$

where r_{TS} is the distance to the termination shock, θ is latitude, ϕ is longitude, r' is the termination shock distance for a given direction normalized to the termination shock distance in the Voyager 2 direction in log space.

Since the termination shock distances used in the hybrid modeling of Giacalone et al. (2021) to determine plasma parameters upstream of the termination shock for the flank and tail direction do not necessarily match the shock distances from our MHD model, we normalize the termination shock distances to the Voyager 2 direction for Equations (6)–(13), such that the parameters used in our ENA modeling for the Voyager 2 direction match the parameters of the ZW7 method for the same direction. To model the unbounded distances (i.e., distances less than the Voyager 2 direction or distances greater than those used for the tail in Giacalone et al. 2021), we set the parameters to be constant and equal to those radial termination shock distances less than that of the Voyager 2 direction and to be constant and equal to those radial termination shock distances greater than that of the tail direction cited in Giacalone et al. (2021). The extrapolated fit results can be seen in Figure 2. Additionally, we ensure that density and thermal energy density from the global MHD solution is conserved within our model, and the fractions follow streamlines from the termination shock to model ENA flux in the heliosheath.

As input to the ENA model, we use the BU MHD model from Kornbleuth et al. (2021). This model uses the same conditions as those used in Izmodenov & Alexashov (2020), and is the same as those used in Gkioulidou et al. (2022). For the BU model, the inner boundary is located at 10 au. Photoionization is neglected and 22 yr averaged solar cycle conditions are used corresponding to the year 1995–2017. Latitudinal variations of the solar wind speed and density are based on interplanetary scintillation data (Tokumaru et al. 2012) and SOHO/SWAN full-sky maps of backscattered Ly α intensities (Qu  merais et al. 2006; Lallement et al. 2010; Katushkina et al. 2013, 2019).

At the outer boundary in the ISM, which is located 1500 au from the Sun, the plasma density (n_p) and neutral hydrogen density (n_{H}) are assumed to be 0.04 and 0.14 cm $^{-3}$. These density values in the ISM, along with the bulk velocity and temperature for the ISM (both plasma and neutrals) of 26.4 km s $^{-1}$ and 6530 K, respectively, are based on the work of Izmodenov & Alexashov (2015) for parameters that best fit the Voyager termination shock distances. The BU MHD model uses an interstellar magnetic field intensity and orientation corresponding to $B_{\text{ISM}} = 3.75 \mu\text{G}$ and $\alpha = 60^\circ$, where the magnetic field is aligned with the hydrogen deflection plane (Lallement et al. 2005) and α is the angle between the interstellar velocity and magnetic field vectors. This direction

and intensity differ from the interstellar magnetic field derived from comparisons with the IBEX ribbon, which assume a secondary ENA population as the source (Schwadron et al. 2009; Zirnstein et al. 2016b), but these values were used by Izmodenov & Alexashov (2020) as they produced the best fits to both the termination shock and heliopause crossings of the Voyager spacecraft with their MHD model.

The results of our ENA modeling are shown in Figure 3. Here, we present 1D cuts along the Voyager 2, flank, and tail directions of the ENA flux for our modeled results based on the ZW7 method and for ENA flux observations from IBEX-Hi and INCA averaged over the years 2009–2012. For IBEX-Hi, we use the ENA flux data from IBEX-Hi Data Release 16, which is in the ram-only direction, and survival probability and Compton–Getting corrected (McComas et al. 2020). For the INCA data, the results are not survival probability corrected or Compton–Getting corrected because ENA emission at energies >5.2 keV becomes essentially optically thin (Dialynas et al. 2017) and the Compton–Getting factor is negligible for ENA intensities at energies >5.2 keV (Roelof et al. 2012; Dialynas et al. 2019). In the tail direction, we only use INCA data from 2009–2011 due to a lack of sky coverage in this region, a technique used to limit ENAs from other sources (Dialynas et al. 2017). It is important to note that the exclusion of the 2012 INCA data from the tail direction, which corresponds to a year with lower flux than the preceding years (Dialynas et al. 2017), inflates the ENA flux data by roughly 15%–20% relative to what it would be were the data available in this direction during the year 2012. We also do not compare model results to INCA data in the flank due to a lack of available data in this region during the years 2009–2012. We sample the model results and data over $15^\circ \times 15^\circ$ bins, and the exact locations probed are shown as black boxes on the global map of Figure 3. Though the simulated solar wind conditions do not necessarily accurately reflect the solar wind data observed from 2009 to 2012, we note that the goal of this study is not to exactly replicate ENA observations, but rather to bridge the gap between ENA models and observations considering Kornbleuth et al. (2018) and Kornbleuth et al. (2020) both required scaling factors of 1.8 to quantitatively compare with IBEX data from 2009 to 2013 despite simulating solar minimum conditions from 2008 in the former and 22 yr averaged solar wind conditions in the latter.

We find that including the separate accelerated PUI population at the termination shock increases the quantitative agreement between the modeled ENA fluxes and data. In previous global ENA modeling efforts using assumed PUI distributions at the termination shock based on the Zank et al. (2010) method (Zirnstein et al. 2017; Kornbleuth et al. 2020, 2021; Shrestha et al. 2021), scaling factors ranging from 1.8 to 2.5 were required to match observations. These methods only included two populations of PUIs: transmitted PUIs and reflected PUIs. Additionally, the ENA modeling used in Gkioulidou et al. (2022), which assumed a transmitted PUI population and a general accelerated PUI population that included reflected PUIs also demonstrated a lack of quantitative agreement with the ENA observations. Here, considering three separate PUI populations, we find good agreement between modeled and observed ENA flux for the 1.11–2.73 keV energy bands for the Voyager 2 and flank directions. It is important to note that because we are using 22 yr averaged solar cycle conditions, we have difficulty matching with the lowest energy

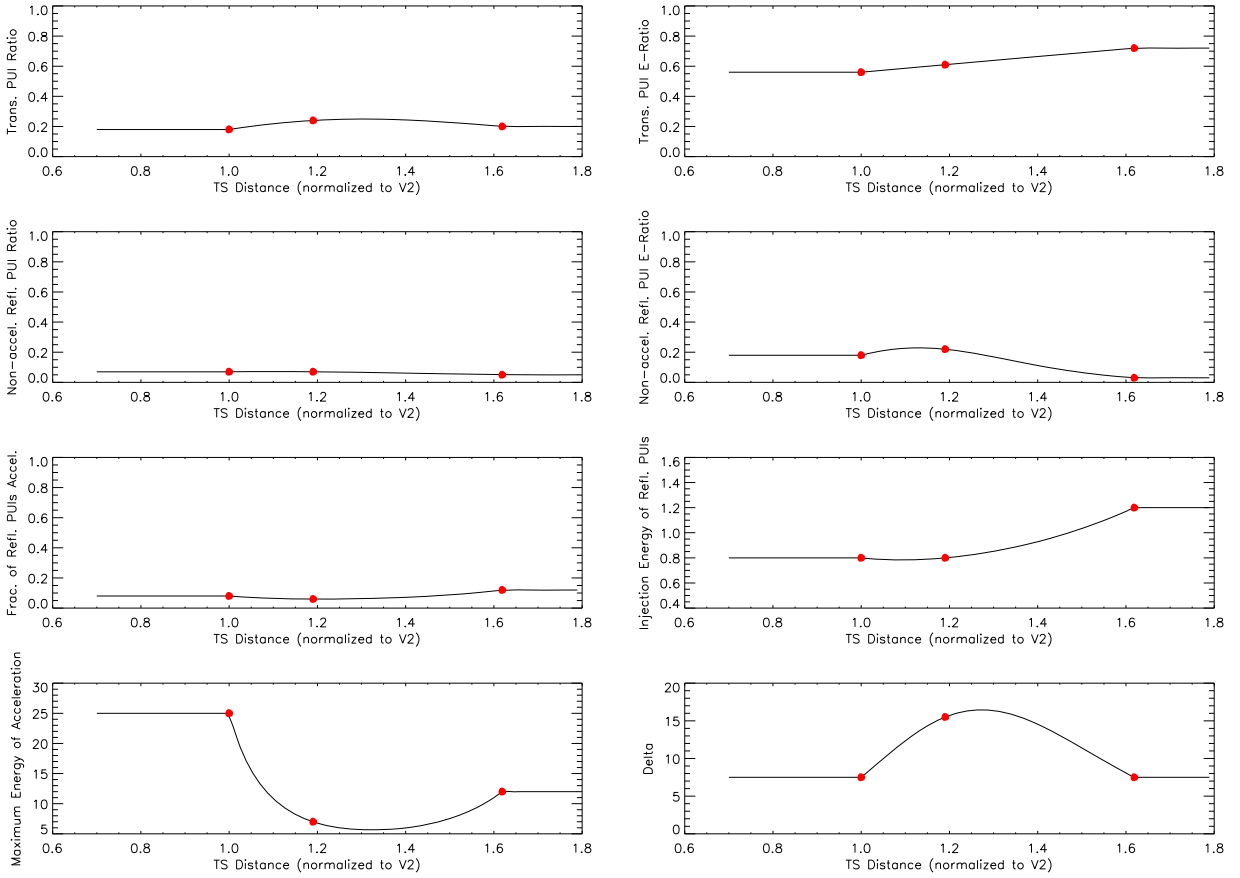


Figure 2. Extrapolated parameters as a function of radial distance to the termination shock normalized to the Voyager 2 direction. The red dots correspond to the best-fit parameters for the ZW7 method for the Voyager 2, flank, and tail directions. From top to bottom, the left column shows the transmitted PUI density fraction relative to the plasma, the reflected PUI density fraction, the fraction of PUIs accelerated at the termination shock, and the maximum energy for reflected PUI acceleration. From top to bottom, the right column shows the transmitted PUI energy fraction relative to the plasma, the reflected PUI energy fraction, the minimum energy for reflected PUI acceleration, and the power-law index (δ) for the accelerated PUIs.

band (0.71 keV) as has been noted previously in Kornbleuth et al. (2021). This is likely due to the large solar wind time period over which our inner boundary conditions are averaged or due to a lack of a time-dependent phenomenon such as corotating interaction regions that would affect data comparisons during solar minimum, which is the period over which we make our comparison.

We note that the value of n_H used in the ISM of 0.14 cm^{-3} leads to a value of 0.101 cm^{-3} for n_H immediately downstream of the upwind termination shock. This is notably less than the New Horizons-derived value from Swaczyna et al. (2020), which predicts a density of $0.127 \pm 0.015 \text{ cm}^{-3}$. Taking the ratio of the lower-limit and median value downstream at the upwind termination shock from Swaczyna et al. (2020) to the value from our model, we note that the ratio ranges from 1.11 to 1.26, which suggests that the results of our comparison are not significantly affected by our choice of n_H within the lower-to-mid limits of Swaczyna et al. (2020). However, if the value of n_H at the termination shock lies near the upper range of the estimate from Swaczyna et al. (2020), we find a ratio of 1.40. In comparison, in Kornbleuth et al. (2021) where the same n_H solution was used as is used here, a scaling factor of 1.8 was required to quantitatively compare with observations. Our value of $n_H = 0.101 \text{ cm}^{-3}$ immediately downstream of the termination shock is also comparable to the inferred average n_H of 0.12 cm^{-3} in the heliosheath along the Voyager 2 direction as found by using INCA and the Voyager 2 Low-Energy

Charged Particle (LECP) instrument data in obtaining the correct heliosheath thickness (Dialynas et al. 2019). Additionally, by using electron plasma oscillations from the Voyager 1 Plasma Wave (PWS) instrument, Gurnett et al. (2013, 2015) inferred that the n_H upstream of the heliopause to be between ~ 0.09 and 0.11 cm^{-3} , which is also comparable with our value of n_H . Therefore, we argue that our conclusions are not affected by our choice of n_H here, especially considering for a majority of energy bands we still show some degree of underprediction—though our results are now more quantitatively comparable as shown in Table 2.

Similar to the work of Gkioulidou et al. (2022), as highlighted in Table 2 we find that from energies of roughly 4–20 keV our model of accelerated PUIs at the termination shock appears insufficient to match observations, likely indicating the presence of additional PUI heating or acceleration in the heliosheath. Additionally, while we do have a good agreement for the Voyager 2 and flank directions, the agreement is less good with increasing termination shock distance, which likewise corresponds to longer heliosheath lines-of-sight. Baliukin et al. (2020) demonstrated the importance of properly modeling the transport of PUIs by including adiabatic heating of PUIs to better match quantitatively with IBEX-Hi observations, although a scaling factor was required for quantitative agreement in their steady-state model. Zirnstein et al. (2018a, 2018b) used the Parker transport equation to model the stochastic acceleration of PUIs in the heliosheath by

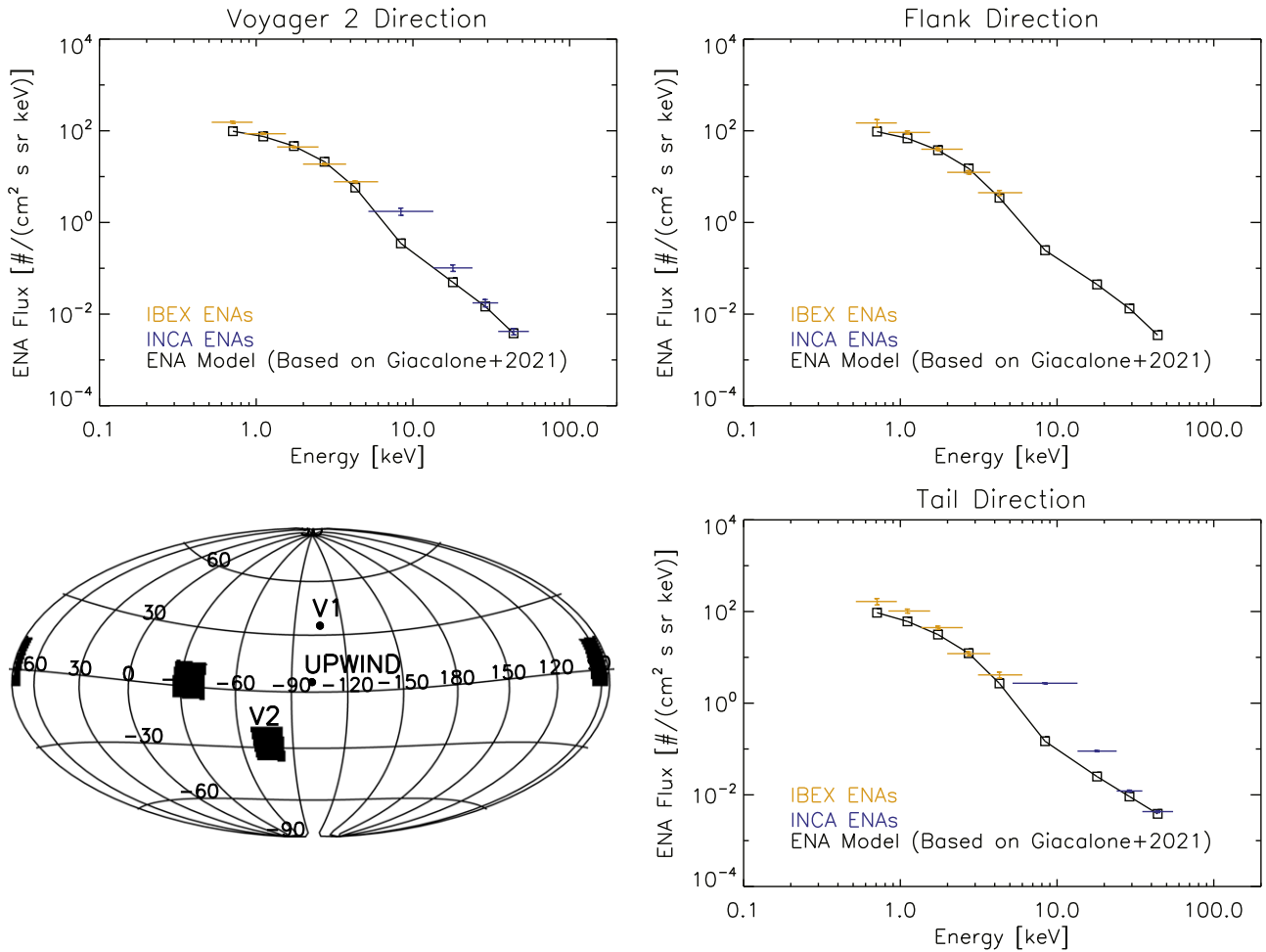


Figure 3. ENA fluxes from the Voyager 2 direction (top left), flank direction (top right), and tail direction (bottom right). The black lines correspond to the modeled ENA flux using the ZW7 method, while the orange and blue lines correspond to the 2009–2012 averages of the IBEX-Hi (orange) and INCA (blue) observations. Bottom left: Global map showing locations of ENA sampling for the figure.

Table 2
Ratios of ENA Flux Between Observations and Models

Energy (keV)	Voyager 2	Flank	Tail
0.71	1.57	1.55	1.76
1.11	1.15	1.34	1.68
1.74	0.95	1.05	1.42
2.73	0.89	0.82	0.98
4.29	1.34	1.29	1.53
8.38	5.00		18.39
18.00	2.06		3.60
28.98	1.20		1.32
43.87	1.10		1.12

Note. Fluxes are averaged over $15^\circ \times 15^\circ$ bins centered on the respective direction.

testing various diffusion rates and ion distributions. Zirnstein et al. (2022) indicated the importance of heating at the termination shock and acceleration of PUIs in the heliosheath, but also required an outer heliosheath population to provide agreement with IBEX-Hi observations. Our results suggest that the heating and acceleration of PUIs both at the termination shock and in the heliosheath is required to replicate ENA observations; however, a quantitative theoretical model is needed before firm conclusions can be drawn. An outer

heliosheath contribution to the ENA flux may also be required based on the amount of PUI acceleration in the heliosheath.

Our results potentially indicate the importance of how proton distributions evolve through a larger heliosheath volume with respect to PUI heating and acceleration in the heliosheath at all energies. This heating and acceleration mechanism seems to have less of an effect in the Voyager 2 direction where the heliosheath thickness is comparatively thin (~ 30 au), and therefore there is less volume over which the proton distributions can evolve, as compared to the flank and tail directions (>50 au) which display an increasing discrepancy with data with increasing heliosheath thickness. For the flank and tail directions, the added effect of the evolving proton distribution is actually limited by the cooling length (i.e., the distance out to which $\sim 37\%$ of ions of a particular energy remain after charge exchange), as this places a limit on how far ENAs can be observed (Schwadron et al. 2014; Zirnstein et al. 2016a; Reisenfeld et al. 2021). Alternatively, an increasing discrepancy with the data may not be related to the heliosheath volume, but related to the heliospheric current sheet (HCS). The Voyager 2 direction tends to lie below the HCS, though Hill et al. (2014) demonstrated that Voyager 2 did at times intersect different sectorized regions created by the oscillating HCS, while the flank and tail directions lie along the ecliptic in the HCS region. McComas & Schwadron (2006) and

Kóta & Jokipii (2008) suggested that the magnetic geometry of the termination shock could lead to further acceleration of PUIs downstream. Zhao et al. (2019) suggested that a potential source of a peak in ACR intensity observed by the Voyager probes approximately 1 au downstream of the termination shock could be magnetic islands formed due to magnetic reconnection in the HCS, which accelerate ions due to Fermi acceleration associated with contracting and interacting magnetic flux ropes/magnetic islands and the reconnection electric field (Zank et al. 2014b). Drake et al. (2010) and Opher et al. (2011) argued that reconnection in the sector region should occur. Therefore, the differences in the data-to-model ENA ratios could be related to the tail direction lying in the HCS, and therefore capturing an additional form of particle acceleration not observed as strongly in the Voyager 2 direction. Additionally, this effect does not appear to be related to the extrapolated parameters in Figure 2, as in the low-latitude tail direction the streamlines should be from those originating at the termination shock for the tail direction given that the flow will deflect to higher latitudes with increasing distance down the tail in the BU model due to the influence of the shortened heliopause given the croissant-like shape.

4. Conclusions

In this work, we present a new model for the production of ENAs via the interaction of the global heliosphere with the ISM, expanding on the basic model of Gkioulidou et al. (2022). As an input to ENA modeling, we replicate hybrid model results of the PUIs at the termination shock for the Voyager 2, flank, and tail directions (Giacalone et al. 2021). To replicate the hybrid results, we use a fitting procedure to infer the different PUI populations present at the termination shock for the IBEX-Hi and INCA energy ranges. We are able to replicate the hybrid results using a Maxwellian approximation for transmitted and reflected PUIs. We introduce a new population of accelerated PUIs considering either two kappa distributions or a diffusively accelerated population of ions based on the model of Wang et al. (2023). The inclusion of an accelerated population of ions accelerated via diffusive shock acceleration best replicates the hybrid results and observed ion fluxes derived from the ENA flux. The accelerated ions correspond to ACRs, with energies >5 keV in the suprathermal tail of the total ion flux, and possess a fraction of the total thermodynamic energy density that ranges from 13% to 22%. Based on these results, the ACRs are a dynamically important population at the termination shock and may well mediate the shock as suggested by Florinski et al. (2010).

The results of this work are significant because they demonstrate through ENAs that DSA is an important physical process for accelerating ions at the termination shock, with ions that have undergone DSA maintaining a non-negligible fraction of the downstream plasma energy. Voyager 1 and 2 observations suggested that DSA was not well observed to occur at the termination shock, although other observations and models (e.g., Florinski et al. (2010)) showed that the termination shock was modified and mediated by ACRs, which suggested DSA as well. Our results with the inclusion of the DSA mechanism in our global model, via selective fitting to DSA-accelerated parts of the hybrid model results, gives entirely new and novel evidence that DSA at the termination shock is likely to be an important physical process—the approach here opens up an entirely new avenue for exploring DSA at the termination shock and inner heliosheath. It also furthers the point that PUI acceleration in the heliosheath is

critical for matching observations considering how DSA generally eliminates the discrepancy between the model and observations at most, but not all, energies.

In modeling the ENA flux, we find that the inclusion of ions beyond 1 keV is sufficient to produce similar levels of ENA flux between the model and observations, which previous ENA modeling without this population was unable to do. This not only suggests the presence of an accelerated PUI population at the termination shock, but also that these populations could strongly contribute to ENA flux production, especially in the IBEX-Hi energies. However, considering the MHD model used corresponds to 22 yr averaged solar cycle data from 1995 to 2017, in the future we will further this investigation using solar wind boundary conditions consistent with the observed time frame to minimize sources of error in our comparison. From ~ 4 to 20 keV, there is a notable discrepancy between modeled ENA fluxes and data, suggesting the possible presence of a heliosheath-accelerated PUI population as well.

The importance of heliosheath acceleration may depend on heliosheath thickness or the cooling length for directions with sufficiently large heliosheath thickness. For the Voyager 2 direction where the observed thickness is 35 au, PUI acceleration at the termination shock appears to be sufficient for replicating the IBEX-Hi observations from 1.11 to 2.73 keV. For the flank and tail directions, which both have thicker heliosheaths along their specific directions, the discrepancy with data increases at these energies despite also being based on the hybrid simulations. Additionally, there may be an acceleration of PUIs in the HCS in the heliosheath (Drake et al. 2010; Opher et al. 2011; Zhao et al. 2019) due to magnetic reconnection, which would have a greater effect on the flank and tail directions that lie in the ecliptic plane than in the Voyager 2 direction that lies in a higher latitude.

The authors were supported by NASA grant 18-DRIVE18_2-0029, Our Heliospheric Shield, No. 80NSSC22M0164. M.K. and M.O. also acknowledge support by NASA HGI grant No. 80NSSC22K0525. G.P.Z., B.W., J.G., and M.G. also acknowledge support from NASA's Interstellar Mapping and Acceleration Probe (IMAP) under NASA contract No. 80GSFC19C0027. G.P.Z. and B.W. acknowledge the partial support of a NASA IBEX grant No. 80NSSC20K0719, subaward SUB 0000395, and an NSF EPSCoR RII-Track-1 Cooperative Agreement OIA—2148653. K.D. also acknowledges support at JHU/APL by NASA under contracts NASS97271, NNX07AAJ69G, and NNN06AA01C and by subcontract at the Office for Space Research and Technology.

ORCID iDs

M. Kornbleuth  <https://orcid.org/0000-0002-3479-1766>
 M. Opher  <https://orcid.org/0000-0002-8767-8273>
 G. P. Zank  <https://orcid.org/0000-0002-4642-6192>
 B. B. Wang  <https://orcid.org/0000-0002-6000-1262>
 J. Giacalone  <https://orcid.org/0000-0002-0850-4233>
 M. Gkioulidou  <https://orcid.org/0000-0001-9979-2164>
 K. Dialynas  <https://orcid.org/0000-0002-5231-7929>

References

- Baliukin, I. I., Izmodenov, V. V., & Alexashov, D. B. 2020, *MNRAS*, 499, 441
 Collier, M. 1995, *GeoRL*, 22, 2673
 Decker, R. B., Krimigis, S. M., Roelof, E. C., & Hill, M. E. 2015, *JPhCS*, 577, 012006

- Dialynas, K., Galli, A., Dayeh, M. A., et al. 2020, *ApJL*, **905**, L24
- Dialynas, K., Krimigis, S. M., Decker, R. B., et al. 2019, *GeoRL*, **46**, 7911
- Dialynas, K., Krimigis, S. M., Decker, R. B., et al. 2022, *SSRv*, **218**, 21
- Dialynas, K., Krimigis, S. M., Mitchell, D. G., et al. 2017, *NatAs*, **1**, 0115
- Drake, J. F., Opher, M., Swisdak, M., & Chamoun, J. N. 2010, *ApJ*, **709**, 963
- Florinski, V., Decker, R. B., & Zank, G. P. 2010, in AIP Conf. Proc. 1216, 12th Int. Solar Wind Conf. (Melville, NY: AIP), 576
- Funsten, H. O., Allegrini, F., Bochsler, P., et al. 2009, *SSRv*, **146**, 75
- Galli, A., Baliukin, I., Bzowski, M., et al. 2022, *SSRv*, **218**, 31
- Giacalone, J., & Decker, R. 2010, *ApJ*, **710**, 91
- Giacalone, J., Nakanotani, M., Zank, G. P., et al. 2021, *ApJ*, **911**, 27
- Gkioulidou, M., Opher, M., Kornbleuth, M., et al. 2022, *ApJL*, **931**, L21
- Gurnett, D. A., Kurth, W. S., Stone, E. C., et al. 2015, *ApJ*, **809**, 121
- Gurnett, D. A., Kurth, W. S., Burlaga, L. F., & Ness, N. F. 2013, *Sci*, **341**, 1489
- Heerikhuisen, J., Pogorelov, N. V., Florinski, V., et al. 2008, *ApJ*, **682**, 679
- Hill, M. E., Decker, R. B., Brown, L. E., et al. 2014, *ApJ*, **781**, 94
- Izmodenov, V. V., & Alexashov, D. B. 2015, *ApJS*, **220**, 32
- Izmodenov, V. V., & Alexashov, D. B. 2020, *A&A*, **633**, L12
- Jokipii, J. R., & Kota, J. 1989, *GeoRL*, **16**, 1
- Jokipii, J. R., & Parker, E. N. 1968, *PhRvL*, **21**, 44
- Katashkina, O., Izmodenov, V., Koutroumpa, D., et al. 2019, *SoPh*, **294**, 17
- Katashkina, O. A., Izmodenov, V. V., Quemerais, E., et al. 2013, *JGRA*, **118**, 2800
- Kleimann, J., Dialynas, K., Fraternali, F., et al. 2022, *SSRv*, **218**, 36
- Kornbleuth, M., Opher, M., Baliukin, I., et al. 2021, *ApJ*, **923**, 13
- Kornbleuth, M., Opher, M., Michael, A. T., et al. 2018, *ApJ*, **865**, 84
- Kornbleuth, M., Opher, M., Michael, A. T., et al. 2020, *ApJL*, **895**, L26
- Kóta, J., & Jokipii, J. R. 2008, in AIP Conf. Proc. 1039, Particle Acceleration and Transport in the Heliosphere and Beyond (Melville, NY: AIP), 397
- Krimigis, S. M., Mitchell, D. G., Roelof, E., et al. 2010, in AIP Conf. Proc. 1302 (Melville: AIP), 79
- Krimigis, S. M., Mitchell, D. G., Roelof, E. C., et al. 2009, *Sci*, **326**, 971
- Lallement, R., Quémerais, E., Bertaux, J. L., et al. 2005, *Sci*, **307**, 1447
- Lallement, R., Quémerais, E., Koutroumpa, D., et al. 2010, in AIP Conf. Proc. 1216, 12th Int. Solar Wind Conf., ed. M. Maksimovic et al. (Melville, NY: AIP), 555
- Lee, M. A., Fahr, H. J., Kucharek, H., et al. 2009, *SSRv*, **146**, 275
- Livadiotis, G., McComas, D. J., Funsten, H. O., et al. 2022, *ApJS*, **262**, 53
- Livadiotis, G., McComas, D. J., Schwadron, N. A., et al. 2013, *ApJ*, **762**, 134
- Malama, Y. G., Izmodenov, V. V., & Chalov, S. V. 2006, *A&A*, **445**, 693
- McComas, D. J., Allegrini, F., Bochsler, P., et al. 2009, *SSRv*, **146**, 11
- McComas, D. J., Bzowski, M., Dayeh, M. A., et al. 2020, *ApJS*, **248**, 26
- McComas, D. J., & Schwadron, N. A. 2006, *GeoRL*, **33**, L04102
- McComas, D. J., Swaczyna, P., Szalay, J. R., et al. 2021, *ApJS*, **254**, 19
- Nakanotani, M., Zank, G. P., Adhikari, L., et al. 2020, *ApJL*, **901**, L23
- Opher, M., Drake, J. F., Swisdak, M., et al. 2011, *ApJ*, **734**, 71
- Opher, M., Loeb, A., Drake, J., et al. 2020, *NatAs*, **4**, 675
- Pogorelov, N. V., Bedford, M. C., Kryukov, I. A., & Zank, G. P. 2016, *JPhCS*, **767**, 012020
- Prested, C., Schwadron, N., Passuite, J., et al. 2008, *JGRA*, **113**, A06102
- Quémerais, E., Lallement, R., Ferron, S., et al. 2006, *JGRA*, **111**, A09114
- Reisenfeld, D. B., Bzowski, M., Funsten, H. O., et al. 2021, *ApJS*, **254**, 40
- Richardson, J. D., Kasper, J. C., Wang, C., et al. 2008, *Natur*, **454**, 63
- Roelof, E., Krimigis, S. M., Mitchell, D. G., et al. 2010, in AIP Conf. Proc. 1302, Pickup Ions throughout the Heliosphere and Beyond (Melville, NY: AIP), 133
- Roelof, E. C., Krimigis, S. M., Mitchell, D. G., et al. 2012, in AIP Conf. Proc. 1436, Physics of the Heliosphere: A 10 Year Retrospective, ed. J. Heerikhuisen et al. (Melville, NY: AIP), 239
- Schwadron, N. A., Bzowski, M., Crew, G. B., et al. 2009, *Sci*, **326**, 966
- Schwadron, N. A., Moebius, E., Fuselier, S. A., et al. 2014, *ApJS*, **215**, 13
- Shrestha, B. L., Zirnstein, E. J., Heerikhuisen, J., et al. 2021, *ApJS*, **254**, 32
- Swaczyna, P., McComas, D. J., Zirnstein, E. J., et al. 2020, *ApJ*, **903**, 48
- Tokumaru, M., Kojima, M., & Fujiki, K. 2012, *JGRA*, **117**, A06108
- Vasyliunas, V. M. 1968, *JGR*, **73**, 2839
- Vasyliunas, V. M., & Siscoe, G. L. 1967, *JGR*, **81**, 1247
- Wang, B., Zank, G. P., Shrestha, B., et al. 2023, *ApJ*, in press
- Zank, G. P., Heerikhuisen, J., Pogorelov, N. V., et al. 2010, *ApJ*, **708**, 1092
- Zank, G. P., Hunana, P., Mostafavi, P., & Goldsten, M. L. 2014a, *ApJ*, **797**, 87
- Zank, G. P., le Roux, J. A., Webb, G. M., et al. 2014b, *ApJ*, **797**, 28
- Zank, G. P., Pauls, H. L., Williams, L. L., et al. 1996, *JGR*, **101**, 21639
- Zhao, L. L., Zank, G. P., Hu, Q., et al. 2019, *ApJ*, **886**, 144
- Zirnstein, E. J., Funsten, H. O., Heerikhuisen, J., et al. 2016a, *ApJ*, **826**, 58
- Zirnstein, E. J., Heerikhuisen, J., Funsten, H. O., et al. 2016b, *ApJL*, **818**, L18
- Zirnstein, E. J., Heerikhuisen, J., Zank, G. P., et al. 2017, *ApJ*, **836**, 238
- Zirnstein, E. J., Kim, T. K., Dayeh, M. A., et al. 2022, *ApJL*, **937**, L38
- Zirnstein, E. J., Kumar, R., Heerikhuisen, J., et al. 2018a, *ApJ*, **860**, 170
- Zirnstein, E. J., Kumar, R., Heerikhuisen, J., et al. 2018b, *ApJ*, **865**, 150